Biology Contribution

Ablative Hypofractionated Radiation Therapy Enhances Non-Small Cell Lung Cancer Cell Killing via Preferential Stimulation of Necroptosis In Vitro and In Vivo

Huan-Huan Wang, MD, PhD,* Zhi-Qiang Wu, PhD,*
Dong Qian, MD, PhD,* Nicholas G. Zaorsky, MD,[†] Ming-Han Qiu, MD,*
Jing-Jing Cheng, MD, PhD,* Chao Jiang, MD,* Juan Wang, MD,*
Xian-Liang Zeng, MD,* Chun-Lei Liu, MD,* Li-Jun Tian, MD,*
Guo-Guang Ying, PhD,[‡] Mao-Bin Meng, MD, PhD,*
Xi-Shan Hao, MD, PhD,[§] and Zhi-Yong Yuan, MD, PhD*

Departments of *Radiation Oncology, CyberKnife Center, and [§]Gastrointestinal Cancer Biology,
[‡]Department of Cancer Cell Biology, Tianjin Medical University Cancer Institute & Hospital, Key
Laboratory of Cancer Prevention and Therapy, National Clinical Research Center for Cancer, Tianjin,
China; [†]Department of Radiation Oncology, Fox Chase Cancer Center, Philadelphia, Pennsylvania

Summary

Our purpose is to investigate how necroptosis, i.e. pro-grammed necrosis, is involved in killing of

Purpose: To investigate how necroptosis (ie, programmed necrosis) is involved in killing of non-small cell lung cancer (NSCLC) after ablative hypofractionated radia-tion therapy (HFRT).
Methods and Materials: Deoxyribonucleic acid damage, DNA repair, and the death form of NSCLC cells were assessed after radiation therapy. The overexpression and

NSCLC after ablative HFRT. This study demonstrated that ablative HFRT at ≥ 10 Gy per fraction induces more necroptosis than apoptosis and that inhibition of RIP3 expression or activity reduces the sensitivity of NSCLC cells to HFRT. We also provide clinical data which suggests that pretreatment tumoral RIP3 expression may provide a predictive marker with which to select patients with favorable responses to SBRT if it can be validated in larger, prospective studies.

silencing of receptor-interacting protein kinases 3 (RIP3, a key protein involved activation of necroptosis)-stable NSCLC cell lines were successfully constructed. The form of cell death, the number and area of colonies, and the regulatory proteins of necroptosis were characterized after radiation therapy in vitro. Finally, NSCLC xenografts and patient specimens were used to examine involvement of necroptosis after ablative HFRT in vivo.

Results: Radiation therapy induced expected DNA damage and repair of NSCLC cell lines, but ablative HFRT at ≥10 Gy per fraction preferentially stimulated necroptosis in NSCLC cells and xenografts with high RIP3 expression, as characterized by induction and activation of RIP3 and mixed-lineage kinase domain-like protein and release of immune-activating chemokine high-mobility group box 1. In contrast, RNA interference of RIP3 attenuated ablative HFRT-induced necroptosis and activation of its regulatory proteins. Among central early-stage NSCLC patients receiving stereotactic body radiation therapy, high expression of RIP3 was associated with improved local control and progression-free survival (all $P < .05$).

Conclusions: Ablative HFRT at ≥10 Gy per fraction enhances killing of NSCLC with high RIP3 expression via preferential stimulation of necroptosis. RIP3 may serve as a useful biomarker to predict favorable response to stereotactic body radiation therapy. © 2018 Elsevier Inc. All rights reserved.

Introduction

Stereotactic body radiation therapy (SBRT), the use of high dose-per-fraction radiation therapy (RT) in 5 fractions or fewer, is a definitive treatment option for peripheral early-stage non-small cell lung cancer (NSCLC). Local recurrence occurs in up to 10% of peripheral lesions (1) and up to 40% of central lesions treated with risk-adapted SBRT (2). There are limited therapeutic options available for the salvage of local failure after SBRT; therefore, the exploration of the mechanisms behind the biology of cell death after SBRT is essential for the development of novel treatment strategies.

Radiation therapy causes cellular death via various pathways, including apoptosis, autophagy, mitotic catastrophe, and necrosis (3). Radiobiological research reveals that low dose-per-fraction regimens (eg, <5 Gy per fraction) provoke mitotic catastrophe, apoptosis, and autophagy; in contrast, high dose-per-fraction regimens (eg, >8-10 Gy per fraction) induce necrosis (4, 5). Cancer cells that evade death by these pathways are typically radioresistant (6), and more research is needed to understand the pathways and exploit them with novel treatment strategies.

Necrosis has been considered an accidental mode of cell death in cancer cells; however, it has recently been recognized that necroptosis, a programmable form of necrosis, may be regulated via defined signal transduction pathways (7). Receptor-interacting protein kinase 3 (RIP3) and receptor-interacting protein kinase 1 (RIP1) are 2 critical kinases responsible for mediating necroptosis (8, 9), and absence of RIP3 contributes to necroptosis resistance (10). Further, the mixed lineage kinase domain-like (MLKL) pseudokinase is a direct executioner of necroptosis (11). Finally, the extracellular chemokine high-mobility group

box 1 (HMGB1) attracts immune cells to cancer cells undergoing necroptosis (12). Thus, RIP3, RIP1, and MLKL activation are currently all synonymous with the onset of necroptosis, and HMGB1 is purported to be involved in subsequent immune response. Accumulating evidence indicates that necroptosis is involved in the regulation of cancer and resistance to subsequent therapy (13-15).

The exploration of tumor cell necroptosis after SBRT will inform our understanding of radiation biology and may be used for clinical decisions. In this study we hypothesized that ablative hypofractionated radiation therapy (HFRT), including SBRT, enhances killing of NSCLC via preferential stimulation of necroptosis. We explored this hypothesis in vitro, by characterizing proteins involved in cellular death of NSCLC treated with ablative HFRT, and in vivo, using NSCLC xenografts and analyzing patients treated with SBRT.

Methods and Materials

Ethics

The animal study was carried out in strict accordance with the recommendations in the Guide for the Care and Use of Laboratory Animals of the National Institutes of Health and our Institutional Animal Care and Use Committee. The clinical protocol was in accordance with the ethical guidelines of the Declaration of Helsinki and was approved by the independent ethics committees at our hospital.

Cell lines and cell culture

The normal lung bronchial epithelial BEAS-2B cell and NSCLC cell lines A549, H520, SPC-A1, H460, H292, and

LTEP-A2 were obtained from American Type Culture Collection (Rockville, MD) and Cell Bank of our institute. Cells at passages 5 to 8 were used for all experiments. Cells were maintained in 1640 medium (Hyclone, Logan, UT) containing 10% heat-inactivated fetal bovine serum (F. Hoffmann-La Roche, Basel, Switzerland), 100 U/mL penicillin, and 100 µg/mL streptomycin (Hyclone) and kept in a humidified 5% CO_2 atmosphere incubator at 37°C.

Establishment of stable transfected cell lines

RIP3-RNAi#1 and RIP3-RNAi#2 and shLacZ, which served as control short hairpin RNA (shRNA), were cloned into pLV-H1-EF1a-puro vector (provided by professor Jia-Huai Han, Xiamen University). The targeting sequences were as follows: RIP3-RNAi#1: GTGGCTAAACAAACTG AATCT; RIP3-RNAi#2: GGGTGCAAGTTGGAGA CAACA; and shLacZ: GTGACCAGCGAATACC TGTTC. The N terminal flag tagged RIP3 coding sequence (CDS) was amplified from pBOB-Flag-hRIP3 (provided by Prof. Jia-Huai Han, Xiamen University) and subcloned into pLVX-IRES-Neo vector. To establish stable transfected cell lines with overexpression or knockdown of RIP3, the indicated plasmids were packed into lentivirus in 293T cells. The infected target cell lines were selected with antibiotics (1 µg/mL for puromycin and 0.5-1 mg/mL for G418).

Cell clonogenic formation assay

Stable transfected NSCLC cell lines or the cells pretreated with 100 µM necroptotic inhibitor necrostatin-1 (Nec-1, the first inhibitor of necroptosis described in the literature (8)) were seeded in 6-well plates (100, 200, 500, 800, 1500, 3000, 5000, and 10,000 cells per well in triplicate, corresponding to the radiation dose of 0, 2, 4, 6, 8, 10, 12, and 15 Gy per fraction, respectively). After overnight incubation, the cells were irradiated with 160-kv X rays using a RS-2000 Biological Irradiatiator (Rad Source Technologies, Buford, GA) at a dose rate of 8.3 Gy/min. The medium was replenished after irradiation. Two weeks later the cells were washed 3 times with phosphate-buffered saline (PBS) to remove cellular debris and were fixed with methanol and stained with 0.1% crystal violet. The number of colonies, defined as ≥50 cells per colony, was counted. The plating efficiency was calculated as the ratio of the number of colonies to the number of plated cells, and the survival fraction was calculated as the normalized plating efficiency to the nonirradiated controls. Next, survival curves were fitted to a linear-quadratic (LQ) model using SigmaPlot 12.0 software (Systat Software, San Jose, CA). The experiments were performed in triplicate to ensure accuracy and precision of the data.

Western blotting analysis

The NSCLC cell lines A549, LTEP-A2, LTEP-A2 with RNAi-RIP3, SPC-A1, or SPC-A1 with RNAi-RIP3 were treated with irradiation at a dose of 0, 2, 4, 10, 15, and 18 Gy per fraction as described above. At time points of 0, 0.5, 1, 2, 4, 6, 8, 16, and 24 hours later, the cells were harvested and lysed in Laemmli sample buffer (Bio-Rad Laboratories, Hercules, CA) or phospho-protein extraction buffer (KeyGEN Biotech, Nanjing, China), followed by centrifuging at $13,000 \times g$ at 4°C for 30 minutes. After measurement of total protein concentrations, the cell lysates (30 µg per lane) were separated on 12% sodium dodecyl sulfate-polyacrylamide gel electrophoresis and transferred to a polyvinylidene difluoride membrane. After blocking with 5% nonfat milk in Tris-buffered saline, 0.1% Tween 20 for 1 hour, the membranes were incubated overnight at 4°C with or without the specific antibodies against H_2AX phosphorylation at Thr139 (γ-H_2AX, #ab2893, abcam, Cambridge, United Kingdom), p53-binding protein 1 (53BP1, #ab36823, abcam), DNA-dependent protein kinase, catalytic subunit (DNA-PKcs, #ab1832, abcam), DNA-PKcs phosphorylation at Thr2609 (#ab18356, abcam), DNA-PKcs phosphorylation at Ser2056 (#ab18192, abcam), ataxia telangiectasia mutated (ATM, #ab199726, abcam), ATM phosphorylation at Ser1981 (#ab79891, abcam), Ku-70 (#ab3114, abcam), Ku-80 (#ab119935, abcam), RIP1 (#ab72139, abcam), RIP3 (#ab152130, abcam), MLKL (#5870, Sigma), MLKL phosphorylation at Ser358 (p-MLKL, #ab187091, abcam), and β-actin (#ab8226, abcam). The bound antibodies were detected with horseradish peroxidase (HRP)-conjugated secondary antibodies (abcam) and visualized using Immobilon Western Chemiluminescent HRP Substrate (abcam).

In addition, the amount of HMGB1 (#ab18256, abcam) in the supernatant of the cell culture was also detected by Western blotting. To ensure accuracy and precision of the data, the experiments were performed in triplicate, and the relative target proteins expression levels were calculated relative to β-actin.

Immunofluorescence staining

The NSCLC cell lines were first seeded in 6-well culture plates and cultivated for 24 hours at 37°C to adhere. Cells were then treated with irradiation as described above. Four hours later the cells were fixed and permeabilized with −20°C cold methyl alcohol for 10 minutes, then blocked in 5% donkey serum in PBS for 1 hour and then co-incubated in a primary antibody DNA-PKcs, p-DNA-PKcs (p-T2609), p-DNA-PKcs (p-S2056), ATM, p-ATM (p-S1981), Ku-70, Ku-80, or RIP3 with the γ-H_2AX in PBS containing 1% bovine serum albumin at 4°C overnight. Then the cells were washed 3 times with PBS to remove cellular debris and incubated with a secondary antibody for 30 minutes. The cells were washed with PBS and stained with 6-diamino-2-phenylindole for 10 minutes and viewed by a confocal laser-scanning microscope (LSM 510 META; Carl Zeiss, Jena, Germany).

In addition, immunofluorescence (IF) doubling staining necrosis marker propidium iodide (PI; BD Pharmingen, USA) and apoptosis marker Venus-based

caspase-3-like protease activity indicator (VC3AI) were used to distinguish apoptosis from necroptosis/necrosis at time points of 0, 3, 6, 12, 24, and 48 hours after a variable dose of irradiation, as previously described (16). For quantification of IF staining, 5 randomly selected tumor cells per slide and 5 slides of each group were observed. The foci in cell nucleus and the integrated optical density values of positive region were objectively assessed under 1000-fold magnification by independent researchers who were blinded to the cellular treatment to ensure accuracy and precision of the data. The integrated optical density of IF images were measured using ImageJ Software (ImageJ 1.37v; National Institutes of Health, Bethesda, MD).

Fluorescence-activated cell sorting

The Annexin V−fluorescein isothiocyanate conjugate (BD Pharmingen, San Jose, CA) and PI binding assay were performed to distinguish apoptosis from necroptosis/necrosis in vitro. A549, A549 cells with overexpression of RIP3, LTEP-A2, LTEP-A2 with RNAi-RIP3, SPC-A1, or SPC-A1 with RNAi-RIP3 were seeded in a 6-well plate. When the cells adhered, the cells were treated with irradiation as described above. After 12 and 24 hours the cells were trypsinized, washed in PBS, and resuspended in binding buffer. Fluorescein isothiocyanate conjugate conjugated Annexin-V and PI were added per the manufacturer's instructions (BD Science, New Jersey, USA). Positive Annexin V staining indicated apoptosis, whereas positive PI staining indicated necroptosis/necrosis. Cells were examined using a flow cytometer (BD FACSArray, BD Biosciences, New Jersey, USA).

Animal and tumor model

Five- to six-week-old female nude mice were matched for weight (20.32 ± 2.03 g) and were obtained from the Experimental Animal Center. The mice were housed in a specific pathogen-free facility with free access to normal chow and water. Twenty-five nude mice were inoculated subcutaneously with LTEP-A2 cells and RIP3-RNAi-LTEP-A2 cells (1×10^6 cells in 0.1 mL of PBS) in the right leg. Perpendicular tumor diameters were measured with a vernier caliper every 2 to 3 days, and tumor volumes were calculated. On day 11, 10 nude mice were excluded if the tumor metastasized, weight and survival status scores did not meet requirements, or the xenograft did not reach 150 to 200 mm³. Then eligible individual mice were randomly and equally assigned to 4 groups (10 in each group): vector, RIP3-RNAi, vector + ablative HFRT (12 Gy per fraction), and RIP3-RNAi + ablative HFRT (12 Gy per fraction).

After index treatments, the body weights and xenograftic growth of eligible mice were measured every other day by 2 independent researchers who were blinded to the animals' treatment, and the xenograftic volumes were calculated using the formula $V = a \times b^2/2$, where a and b are the largest and smallest xenograftic diameter, respectively. The mice were killed, and the xenograftic weights were also assessed. Each experiment was performed in triplicate.

Before ablative HFRT, mice were anesthetized with chloral hydrate and then restrained on an acrylic board with adhesive tape. With a lead board shielding the mice bodies, only the tumor-bearing legs were irradiated locally at the center of the 24×2-cm field. Ablative HFRT was delivered via a precision 6-MV photon beam from a linear accelerator at a dose rate of 4.0 Gy/min (1232 Medical Linear Accelerator; Elekta, Stockholm, Sweden). A 1.0-cm bolus was used to achieve homogeneous dose deposition in the xenografts.

Inclusion and exclusion criteria of xenograftic nude mice were described above. When tumor volume reached 150 to 200 mm³, eligible mice were randomly and equally divided into variable doses of RT, with 10 mice in each RT arm. Then the tumor-bearing legs were irradiated. Thereafter, eligible mice were killed by cervical dislocation, 4 hours after RT. Using the xenograftic tissues and blood samples, further analyses were performed focusing on changes in the form of cell death and immunity activation potential, as well as its intrinsic mechanisms.

Enzyme-linked immunosorbent assay

The NSCLC xenografts were exposed to various doses of RT, the blood samples from xenograftic mice were centrifuged at 3000 rpm for 5 minutes at 4°C, and the separated serum samples were stored at −20°C until use for assay. Levels of HMGB1 were measured using the monoclonal anti-mouse antibody (R&D Systems, Minneapolis, MN) according to the manufacturer's instructions. Calibration curves were established, and each microtiter plate with a standard curve. The colorimetric reaction was read with a Benchmark Microplate Reader (Benchmark Electronics, Angleton, TX).

Transmission electronic microphotography

Transmission electronic microphotography was performed to identify the NSCLC cell death morphology after ablative HFRT; the xenograftic tissues from an individual group of mice were dissected. The xenograftic tissues were superfused with 3% glutaraldehyde. The xenografts were sliced into blocks with faces of 1 to 2 mm² and fixed by immersion in the same fixative for 72 hours at 4°C. The blocks were then rinsed twice in PBS containing 0.2 M sucrose and postfixed in 1% osmium tetroxide, dehydrated in an ascending series of acetone, cleared in propylene oxide, and embedded in Epon812. At least 3 blocks per xenograft were chosen at random, and semi-thin sections of 1-mm³ thickness were cut. Each block was further trimmed to ultra-thin sections of 50-nm thickness and stained with uranyl acetate and lead citrate. The sections were observed with a transmission electron microscope (H600 electron microscope; Hitachi, Tokyo, Japan) at an accelerating voltage of 75 kV.

Treatment schedule and tumor control of eligible NSCLC patients

To explore the role of RIP3 expression in tumor control of central early-stage NSCLC patients after SBRT, eligible patients were selected from our CyberKnife Center. All patients were screened and enrolled in the present study by oncologists according to the following criteria: (*1*) any age; (*2*) Karnofsky performance score ≥70; (*3*) diagnosed with NSCLC on the basis of histopathologic examinations; (*4*) clinical T1-2 N0 M0, according to either computed tomography (CT) and/or positron emission tomography (PET)-CT examinations; (*5*) unamenable to resection either because of anatomic tumor characteristics, patient comorbidities, or refusal; (*6*) central lesion, defined as a tumor within 2 cm in all directions around the proximal bronchial tree and immediately adjacent to mediastinal or pericardial pleura as in Radiation Therapy Oncology Group protocol 0813 (17, 18); and (*7*) informed about the potential benefits and risks of SBRT, with written informed consent.

All included patients were seen in follow-up 1 month after completion of SBRT, then every 3 months for the first year, then 6 months until July 2016. Imaging, adverse events, and compliance of all patients were monitored for the follow-up period using our clinical database. The primary endpoint was local control (LC), defined as no progression of treated disease on follow-up scans, with complete response, or partial response, or stable disease, defined using the Response Evaluation Criteria in Solid Tumors (RECIST 1.1). The secondary endpoints were: (*1*) overall survival (OS), defined as the time between the date of the SBRT and the date of death or the date of the last follow-up for censored patients; and (*2*) progression-free survival (PFS), defined as the time between the date of the SBRT and the date of disease progression or the date of the last follow-up for censored patients.

Given patient comorbidities and the relatively unreliable negative predictive value of biopsy, tissue diagnosis of failure was not always possible or necessary. The following high-risk features were suggestive of local failure: (*1*) enlarging opacity at primary site; (*2*) sequential enlarging opacity; (*3*) enlarging opacity after 12 months; (*4*) bulging margin; (*5*) loss of linear margin; and (*6*) air bronchogram loss. A PET-CT scan was used to assist with differentiating radiation-related changes from local or regional recurrence. A local recurrence was classified as having at least 3 high-risk features and a PET-CT standardized uptake value >2.5 or >3 high-risk features without PET-CT (19). Local failure was assessed carefully after SBRT, to avoid uncertainty associated with early transient radiographic changes within the high-dose region.

Immunohistochemical assay and evaluation

The expression of MLKL phosphorylation at Ser358 (p-MLKL, #ab187091, abcam) and RIP3 in tumor tissues of mice and patients' NSCLC specimens were determined by immunohistochemical (IHC) analysis. Briefly, the tumor tissues from an individual group of mice and included patients before treatment were obtained, and then tissue sections at 4 μm were rehydrated, treated with 3% H_2O_2, and blocked with 3% bovine serum albumin. Subsequently the tissue sections were incubated with anti-RIP3 antibody and anti-p-MLKL at Ser358 or with control immunoglobulin G overnight at 4°C. The bound antibodies were detected with HRP-conjugated second antibodies and Diaminobenzidine (DAB), followed by imaging under a light microscope.

The expression levels of p-MLKL and RIP3 in tumor tissues of mice and patient specimens were assessed by 4 independent physician scientists who were blinded to clinical follow-up data. Their conclusions were in complete agreement for 85% of cases, indicating that this scoring method was highly reproducible. If 3 or all 4 agreed with the scoring results, the value was selected. If there was a disagreement (2 agreeing vs 2 disagreeing), then the pathologists worked collaboratively to confirm the score.

For evaluation of RIP3 staining, a semi-quantitative scoring criterion was used, in which both staining intensity and positive areas were recorded. A staining index (values 0-16) obtained as the intensity of positive staining (weak, 1; moderate low, 2; moderate high, 3; strong, 4) and the proportion of positive cells of interest (0%, 0; <10%, 1; 10%-50%, 2; 51%-80%, 3; >80%, 4) were calculated. Finally, cases were classified into 2 different groups: low expression cases (score 0-8) and cases with high expression (score 9-16).

Statistical analyses

Continuous variables were expressed as the mean ± standard deviation, and these were compared using an unpaired Student *t* test and linear regression analysis. Xenograftic regrowth was compared using repeated measures one-way analysis of variance. Local control, OS, and PFS curves were estimated using Kaplan-Meier analysis and compared using the stratified log-rank test. The differences with $P < .05$ (2-tailed) were considered statistically significant. Data were analyzed using the statistical software Intercooled Stata version 8.2 for Windows (StataCorp, College Station, TX).

Results

The difference in *LQ* model—estimated isoeffective NSCLC survival after ablative HFRT

We first tested the appropriateness of the *LQ* model to describe isoeffective survival of NSCLC cell lines, including A549, LTEP-A2, and SPC-A1, after variable RT doses. The A549 cells conformed closely to those of the *LQ* model; however, the *LQ* model underestimates doses for isoeffective LTEP-A2 and SPC-A1 cell survival with
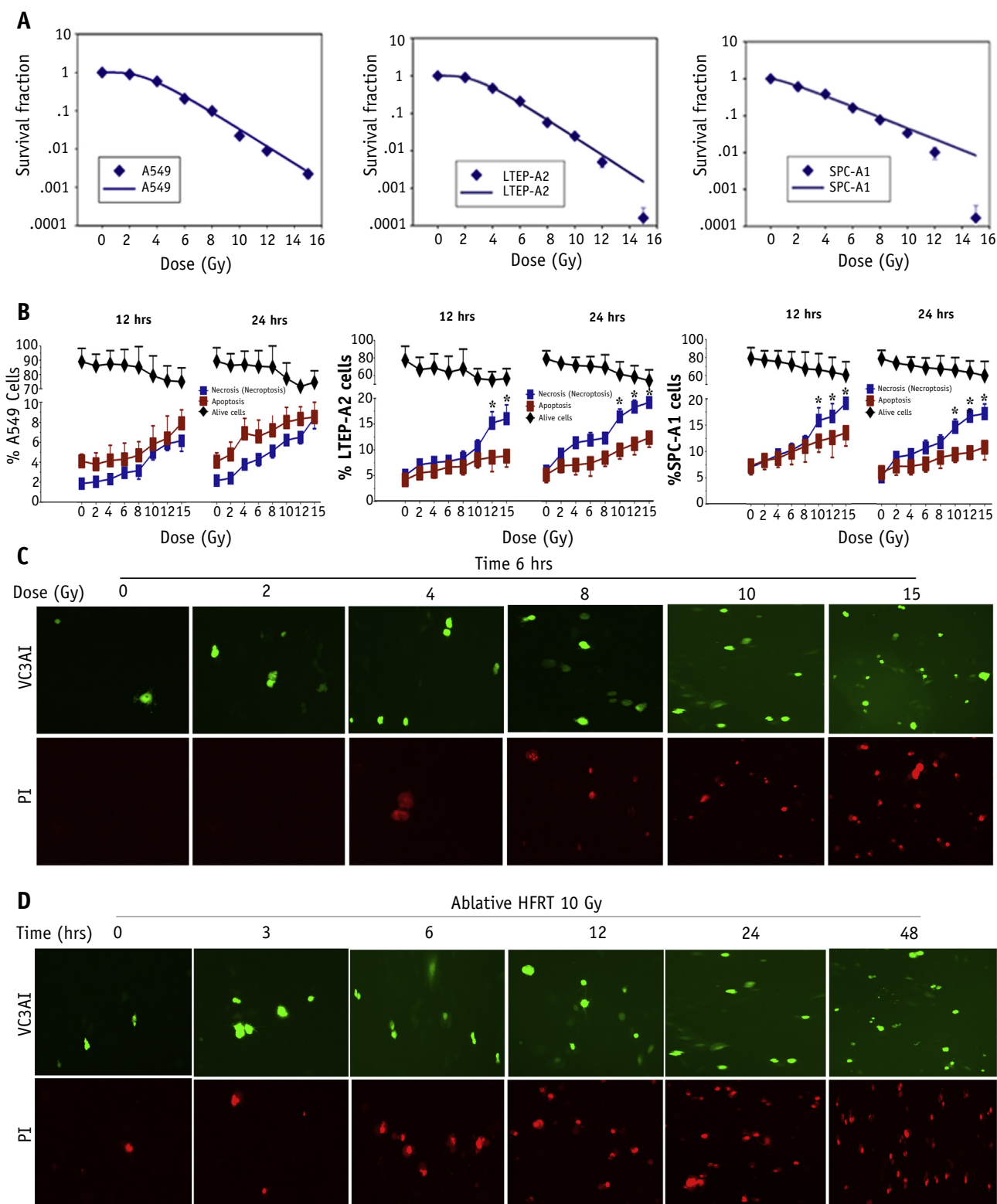
Fig. 1. The radiosensitivity of NSCLC cells were performed and HFRT at ≥10 Gy per fraction preferentially stimulated necroptosis in NSCLC cells. (A) The NSCLC cell lines A549, LTEP-A2, and SPC-A1 were exposed to 0, 2, 4, 6, 8, 10, 12, and 15 Gy per fraction as indicated. After 14 days, colonies were stained and colony numbers were counted. (B) The NSCLC cell lines were treated with various doses of radiation therapy at 12 and 24 hours; then, fluorescence-activated cell sorting using Annexin-V/propidium iodide (PI) double staining determined cell death forms. Apoptosis: Annexin-V−positive cells; necrosis: PI-positive cells. The data are presented as mean ± standard deviation. (C-D) LTEP-A2 cells were exposed to various doses of radiation therapy 6 hours later or 10 Gy per fraction at different times, ranging from 0 to 48 hours later, then cells were stained with PI and VC3AI under a fluorescence microscope at 10 × 40. *P < .05 versus apoptosis.

ablative dose at ≥ 10 Gy per fraction (Fig. 1A and Fig. E1 [available online at www.redjournal.org]). These findings suggest that there may be in part different intracellular mechanisms of DNA damage and corresponding DNA repair with ablative doses of ≥ 10 Gy per fraction (vs < 10 Gy per fraction) among these cells.

RT-induced similar DNA double-strand breaks and nonhomologous end-joining repair of NSCLC cells in vitro

Radiation therapy mainly induces DNA double-strand breaks (DSBs) and corresponding DNA nonhomologous end-joining (NHEJ) repair. We addressed whether there was a difference in DNA DSBs and DNA NHEJ repair among NSCLC cell lines after variable RT doses; our results revealed that RT significantly induced γ-H$_2$AX and 53BP1 foci formation in a dose-dependent manner (Figs. E2A-C and E3A and E3B; available online at www.redjournal.org).

Correspondingly, exposure to RT significantly recruited a robust phosphorylation of DNA-PKcs at Thr2609 and Ser2056, as well as phosphorylation of ATM at Ser1981 into the DNA damage site for corresponding repair other than DNA-PKcs, ATM, Ku-70, and Ku-80 in NSCLC cell lines (Figs. E2B and E2D, E3A, and E3C-I; available online at www.redjournal.org). Taken together, these results suggested that RT induces similar DNA DSBs and corresponding NHEJ repair in NSCLC cell lines, and the difference in *LQ* model estimates at high dose-per-fraction RT (ie, ≥ 10 Gy per fraction) in part may be due to different mechanisms of cell death forms except for other causes.

Ablative HFRT preferentially stimulated necroptosis in NSCLC in vitro

Fluorescence-activated cell sorting analyses and IF double staining with PI and VC3AI exhibited an apparent increase in both apoptosis and necroptosis among NSCLC cells treated with RT at < 10 Gy per fraction in a dose-dependent manner. However, ablative HFRT with doses ≥ 10 Gy per fraction resulted in killing of NSCLC cells via preferential stimulation of necroptosis in LTEP-A2 and SPC-A1 cell lines but not A549 cells (Fig. 1B-D).

Ablative HFRT–induced necroptosis in an RIP3-dependent manner in vitro

To test the role of RIP3-dependent necroptosis in the sensitivity of NSCLC cell lines treated with RT, the expression levels of RIP3 and RIP1 in BEAS-2B and 6 NSCLC cell lines (A549, H520, SPC-A1, H460, H292, and LTEP-A2) were evaluated by Western blot assays. RIP1 had similar moderate expression among these cell lines; in contrast, RIP3 expression was higher in BEAS-2B, LTEP-A2, and SPC-A1. Conversely, there was almost no RIP3 expression in A549, H520, H460, and H292 (Fig. 2A).

Importantly, RT resulted in an RIP3 induction and γ-H$_2$AX foci formation in a dose-dependent manner, although the induction may vary among cell lines (Fig. 2C and Fig. E4 [available online at www.redjournal.org]). These data suggest that ablative HFRT-induced RIP3 might be companied by γ-H2AX foci formation.

Next we successfully constructed A549 cells with overexpression of RIP3, LTEP-A2, and SPC-A1 cell lines with RNAi-RIP3, corresponding controls, and parental lines. After demonstrating the authenticity, the expression levels of RIP3 in 3 cell lines were tested by Western blot assays. Transfection with control plasmid did not significantly modulate RIP3 expression, as expected; transfection with overexpression of RIP3 increased the expression of RIP3 in A549 cells, whereas RNAi-RIP3 reduced the expression of RIP3 in LTEP-A2 and SPC-A1 cell lines (Figs. 2B and 2C).

We used necroptotic inhibitor Nec-1, RIP3 overexpression in A549, or RIP3 silencing in LTEP-A2 and SPC-A1 cell lines at ablative HFRT, 10 Gy per fraction, to determine necroptosis and apoptosis levels at different times. RIP3 overexpression significantly increased necroptosis in A549 cells. In contrast, Nec-1 and RNAi-RIP3 significantly decreased necroptosis after ablative HFRT in LTEP-A2 and SPC-A1 cell lines but not in A549 cells (Fig. 2D-F).

RIP3-dependent necroptosis impacted the radiosensitivity of NSCLC cells to ablative HFRT in vitro

To further validate RIP3 overexpression or silencing on their radiosensitivity, colony formation analyses showed that the number of colonies formed by RNAi-RIP3 cells was significantly increased compared with that of control cells in LTEP-A2 and SPC-A1 with ablative HFRT at higher doses, ≥ 10 Gy per fraction (all $P < .05$); however, the number of colonies formed by overexpression of RIP3 cells was significantly decreased compared with that of control cells in the A549 cell at ablative doses of HFRT, ≥ 10 Gy per fraction ($P < .05$). Similarly, the number of colonies formed in LTEP-A2 and SPC-A1 cells pretreated with Nec-1 was significantly increased compared with that of control cells at ablative doses of HFRT of ≥ 10 Gy per fraction (all $P < .05$); however, there was no significant change in the amount of necroptosis in A549 cells pretreated with Nec-1 compared with control cells at any dose of RT ($P > .05$).

Interestingly, transfection with plasmid and pretreatment with Nec-1 of LTEP-A2 and SPC-A1 cell lines revealed that they conformed closely to those of the *LQ* model; in contrast, the A549 cells did not (Fig. 2G-L). These data suggest that interference of RIP3 expression decreases the radiosensitivity of NSCLC cell lines at ablative doses of HFRT, ≥ 10 Gy per fraction and that necroptosis may in part cause cell death, which was not explained by the classic radiobiological *LQ* model.
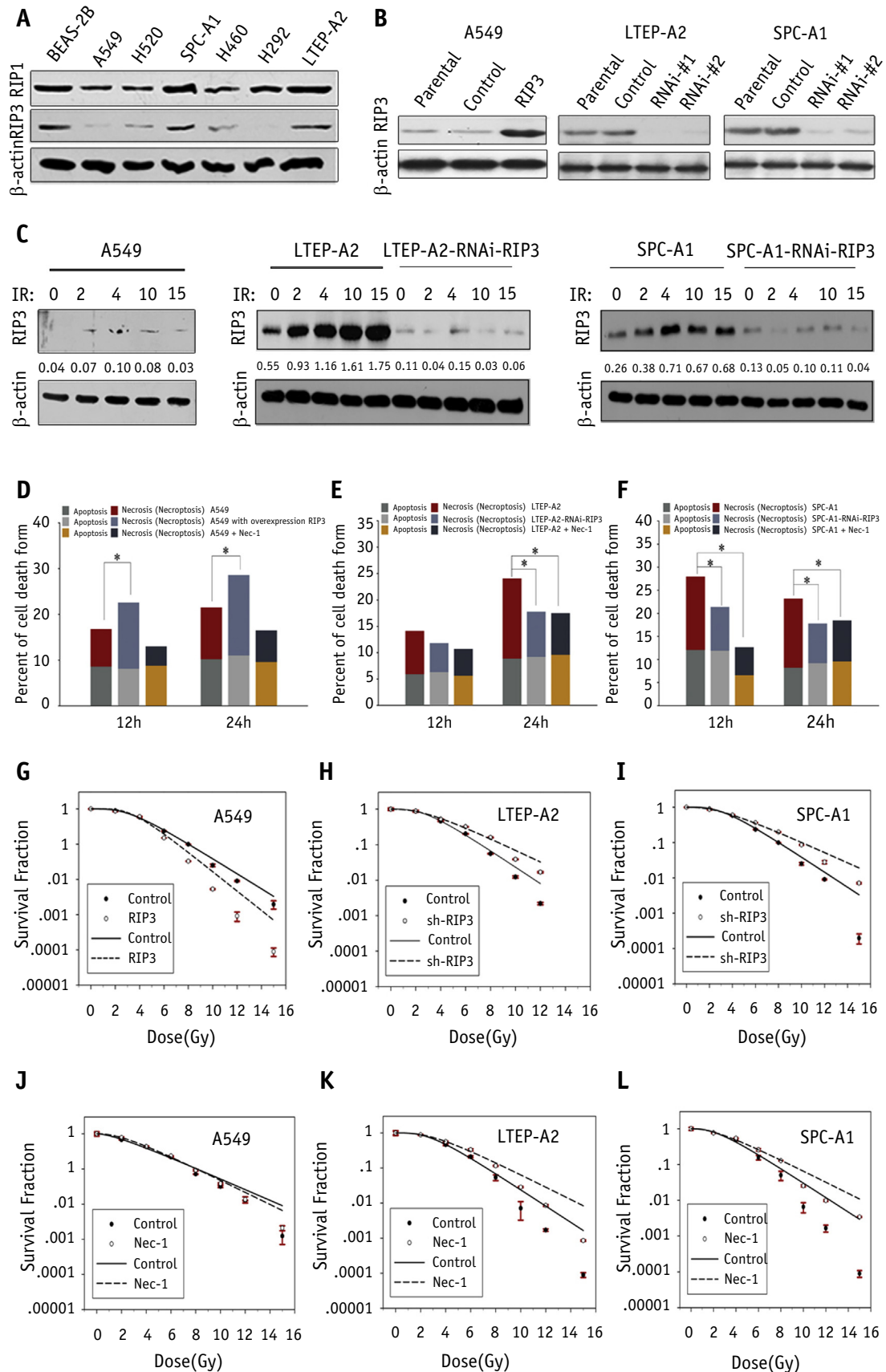
Fig. 2. Ablative hypofractionated radiation therapy (HFRT) induces necroptosis in a RIP3-dependent manner. Knockdown of RIP3 or use of the necroptotic inhibitor Nec-1 induces ablative HFRT resistance by attenuating necroptosis in vitro. (A) RIP3 and RIP1 endogenous expression levels in normal lung bronchial epithelial cells BEAS-2B and 6 non-small cell lung

Knockdown of RIP3-induced ablative HFRT resistance by attenuating necroptosis in vivo

To determine the effect of RIP3 silencing on the radio-sensitivity in vivo, nude mice were inoculated subcutaneously with 1×10^6 LTEP-A2 cells and LTEP-A2 with RNAi-RIP3. When the implanted tumors grew to 150 to 200 mm^3 in volume, the mice were randomized with vector, RIP3-RNAi alone, vector + ablative HFRT (12 Gy per fraction), or RIP3-RNAi + ablative HFRT (12 Gy per fraction). The body weights and the growth of xenografts in individual mice were monitored longitudinally, and the body weights in different groups of mice were evaluated at individual time points.

The xenograftic tissues were dissected, and transmission electronic microphotography revealed that apoptotic cells exhibited morphologic and biochemical characteristics including condensation of cytoplasm, chromatin marginalization, nuclear fragmentation, and externalization of phosphatidyl-serine on the cell surface. In contrast, necroptotic cells were characterized by extensive vesiculation of cytoplasmic organelles, dilation of the endoplasmic reticulum elements, cytoskeletal degradation, and rupture of plasma membrane (Fig. 3A).

Furthermore, treatment with control plasmid and RIP3-RNAi alone did not affect the growth of xenografts, whereas ablative HFRT or ablative HFRT with RIP3-RNAi significantly inhibited the growth of xenografts in nude mice (all $P < .05$; Figs. 3B and 3C). Similarly, increases in xenograftic weight and growth were observed in mice treated with RIP3-RNAi + ablative HFRT compared with single ablative HFRT treatment ($P < .05$; Fig. 3B-D). These data suggest that knockdown of RIP3 attenuates necroptosis after ablative HFRT in vivo.

MLKL induction and activation as well as the release of HMGB1 were involved in ablative HFRT-induced necroptosis in vitro and in vivo

Activation of MLKL was identified as a critical downstream effector of RIP3 during the execution of necroptosis. In multiple cell lines there was no endogenous MLKL expression, whereas HMGB1 had moderate endogenous expression in BEAS-2B and 6 NSCLC cell lines (Fig. 4A). The treatment of LTEP-A2 cells with ablative HFRT resulted in a robust MLKL induction, phosphorylation at Ser358, and trimerization, as well as release of HMGB1; however, MLKL induction and activation as well as release of HMGB1 were significantly decreased in A549 cells and LTEP-A2 cells with RNAi-RIP3 (Figs. 4B and 4C and 5A-C).

Additionally, nude mice were inoculated subcutaneously with 1×10^6 LTEP-A2 cells, and when the implanted tumors grew to 150-200 mm^3 in volume, LTEP-A2 xenografts were treated with variable doses of RT. Then the xenograftic tissues were dissected, and IHC assay revealed that RT resulted in RIP3 and MLKL phosphorylation in a dose-dependent manner in LTEP-A2 xenografts (Fig. 4D).

The extracellular chemokine HMGB1 attracts immune cells to cancer cells undergoing necroptosis. Enzyme-linked immunosorbent assay showed that RT significantly induced release of HMGB1 in a dose-dependent manner. In contrast, the release of HMGB1 was significantly decreased in A549 and LTEP-A2 cells with RNAi-RIP3 xenografts in vivo (Fig. 5D). These data suggest that MLKL induction and activation as well as release of HMGB1 are involved in ablative HFRT-induced necroptosis in vitro and in vivo.

RIP3 and necroptosis were associated with clinical outcomes of NSCLC patients after SBRT

To examine whether RIP3 and necroptosis were associated with clinical outcomes of eligible central early-stage NSCLC patients after SBRT, the pretreatment RIP3 expression levels were analyzed by IHC assays. Among these patients, high expression of RIP3 was associated with improved LC and PFS after SBRT (all $P < .05$; Fig. 6A-D). Patients with high expression of RIP3 had a non-statistically significant trend toward improvement in OS (50 months vs 29 months), which might be limited by the sample size. Additionally, characteristics of patients with local recurrence are summarized in Table E1 (available online at www.redjournal.org). These data suggest that RIP3 expression and necroptosis are associated with the clinical outcomes of central early-stage NSCLC patients receiving SBRT.

cancer cell lines, including A549, H520, SPC-A1, H460, H292, and LTEP-A2, were evaluated by Western blot assays. (B) The plasmids of over expression of RIP3 in A549 cells as well as RNAi-RIP3 in LTEP-A2 and SPC-A1 cell lines, control, and parental were successfully constructed. (C) Non-small cell lung cancer cells were exposed to various doses of radiation therapy; 4 hours later, RIP3 expression levels were evaluated by Western blot assays. (D-F) Effects of RIP3 overexpression or silencing as well as the necroptotic inhibitor Nec-1 on the form of cell death after ablative HFRT in vitro. The cells were exposed to 10 Gy per fraction as indicated. After 12 and 24 hours, fluorescence-activated cell sorting using Annexin-V/propidium iodide double staining determined cancer cell death forms. (G-I) Effects of RIP3 overexpression or silencing on radiosensitivity in vitro. The cells were exposed to 0, 2, 4, 6, 8, 12, and 15 Gy per fraction of radiation therapy as indicated. After 14 days, colonies were stained, and colony numbers were counted. Knockdown or overexpression of RIP3 interferes with ablative HFRT sensitivity by attenuating or inducing necroptosis in vitro in the 3 cell lines tested, A549, LTEP-A2, and SPC-A1. (J-L) The necroptotic inhibitor Nec-1 induces ablative HFRT resistance by attenuating necroptosis in LTEP-A2 and SPC-A1 cells but not in A549 cells. *$P < .05$.
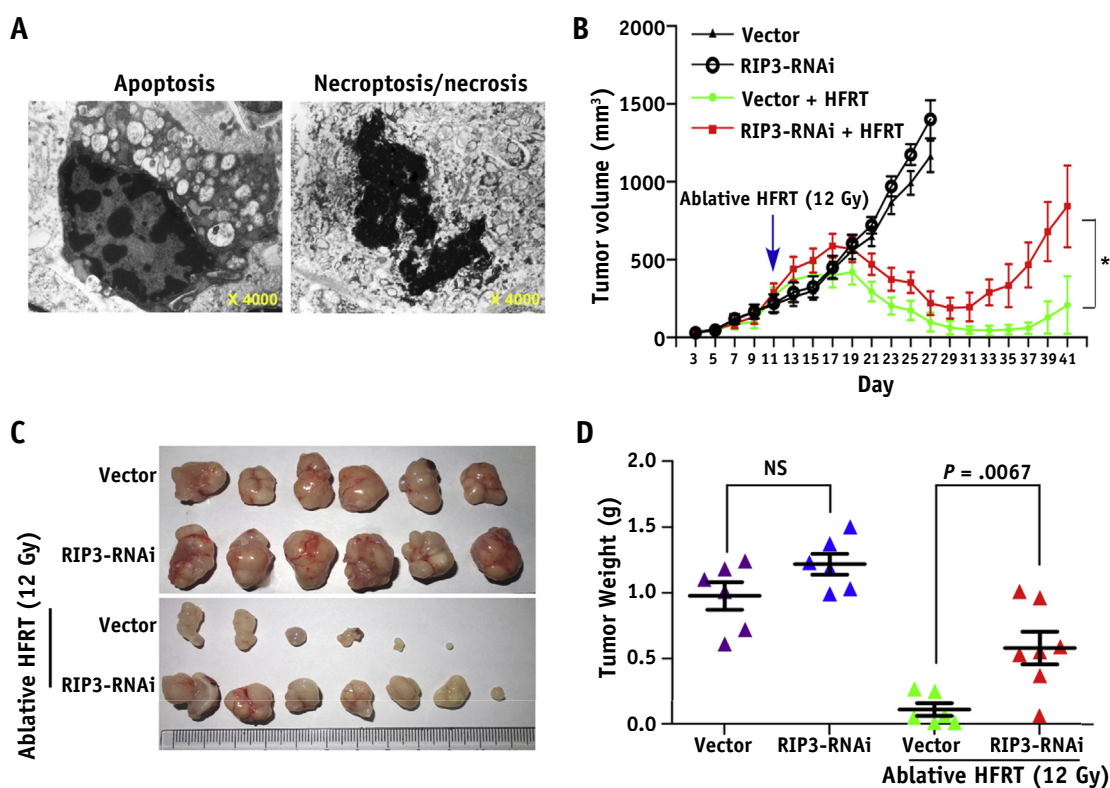
Fig. 3. Knockdown of RIP3 attenuates necroptosis after ablative hypofractionated radiation therapy (HFRT) in vivo. Nude mice were inoculated with LTEP-A2 cells and LTEP-A2 with RNAi-RIP3 cells, and when the xenografts grew to 150 to 200 mm^3 in volume, the nude mice were randomized to treatment with vector, RIP3-RNAi alone, vector + ablative HFRT (12 Gy per fraction), and RIP3-RNAi + ablative HFRT (12 Gy per fraction). The body weights and xenografts growth of individual mice were monitored longitudinally. (A) Transmission electronic microphotography was performed to identify the cancer cell death morphology after ablative HFRT. (B, C) The xenograftic growth curve in vivo. (D) The xenograftic weights of mice. *$P < .05$ versus vector + ablative HFRT group.

Discussion

The *LQ* model has been the dominant model used to predict cell survival in clinical situations; however, it is unknown whether this model is appropriate for ablative high dose-per-fraction (eg, >8-10 Gy per fraction) RT (20-23). We characterized NSCLC cell death after ablative HFRT to find alternative mechanisms of cell death not explained by the *LQ* model (24, 25). Our results suggest that ablative HFRT at ≥10 Gy per fraction enhances killing of NSCLC with high RIP3 expression via preferential stimulation of necroptosis, as characterized by induction and activation of RIP3 and MLKL protein, and release of immune-activating chemokine HMGB1. Further, RIP3 may serve as a useful biomarker to predict favorable response to SBRT if it can be validated in larger, prospective studies (Fig. 6E).

In contemporary radiobiology, DNA DSBs are recognized as the most biologically important form of damage caused by RT; our data were consistent with these findings when using conventionally fractionated RT. After conventionally fractionated RT, we noted the expected robust phosphorylation of DNA-PKcs at Thr2609 and Ser2056, as

well as ATM at Ser1981 to repair DNA DSBs in vitro. However, because induction in DNA DSBs and corresponding NHEJ repair is similar in 3 NSCLC cell lines, we speculated that the difference in *LQ* model estimates and NSCLC patient survival after ablative HFRT might be in part due to different mechanisms, including vascular/stromal endothelial damage, antitumor immunity activation, the eradication of subpopulations of tumor stem cells, and necroptosis (26, 27).

Accumulating evidence indicates that necroptosis is involved in the regulation of cancer therapy (13-15), and further insights into the cancer cell death patterns will likely have important implications in tumors treated with RT (28). We therefore focused on the cell death forms accompanied by radiation dose enhancement, and our findings showed an apparent increase in both apoptosis and necroptosis among NSCLC cells treated with RT at <10 Gy per fraction in a dose-dependent manner. However, ablative HFRT with doses of ≥10 Gy per fraction resulted in killing of NSCLC cells via preferential stimulation of necroptosis in LTEP-A2 and SPC-A1 cell lines. These results are consistent with previous studies (4, 5), suggesting that lower radiation therapy doses used in conventionally and
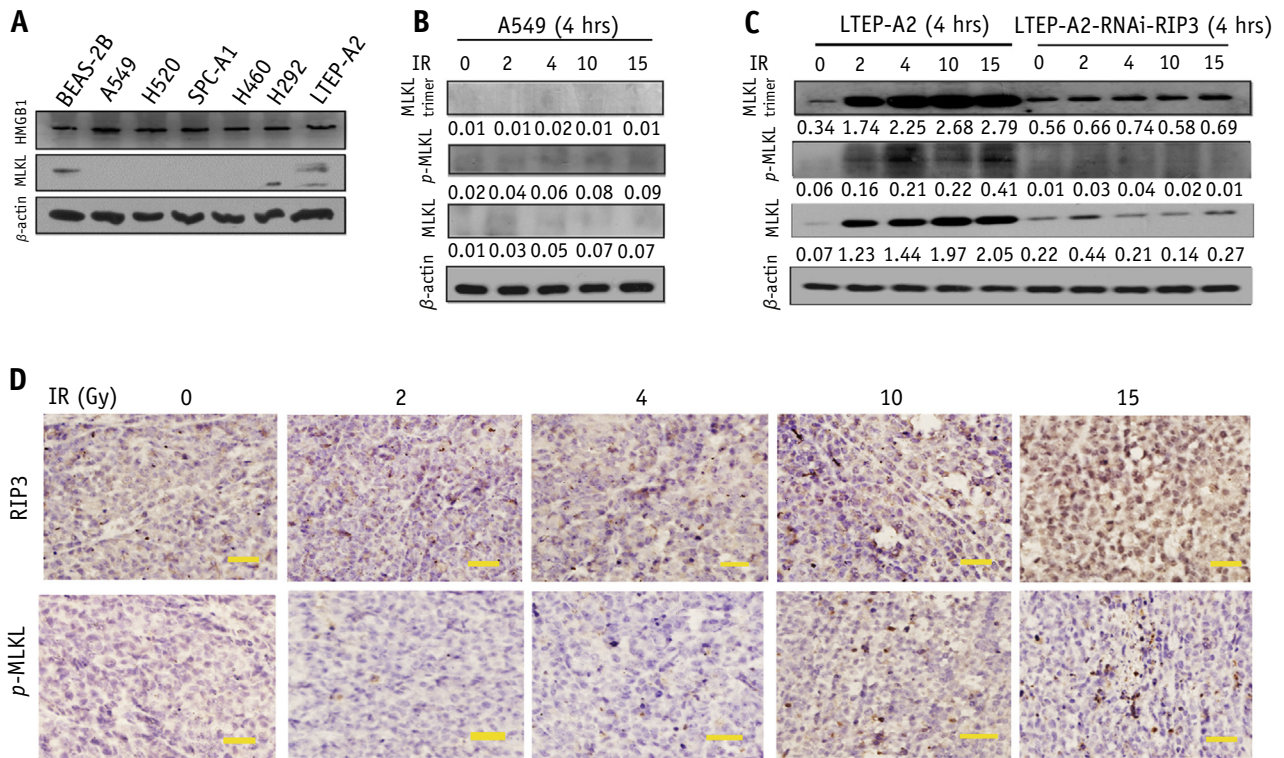
Fig. 4. Induction and activation of MLKL as well as release of HMGB1 were involved in ablative hypofractionated radiation therapy—induced necroptosis in vitro and in vivo. (A) Endogenous expression of MLKL and HMGB1 was evaluated by Western blot assays in BEAS-2B, A549, H520, SPC-A1, H460, H292, and LTEP-A2. (B, C) A549, LTEP-A2, and LTEP-A2 with RNAi-RIP3 cells were exposed to various doses of radiation therapy; next, MLKL induction, p-MLKL, and MLKL trimerization expression levels were evaluated by Western blot assays. (D) LTEP-A2 xenograftic tissues were dissected after ablative hypofractionated radiation therapy, and the expression levels of RIP3 and p-MLKL in tumor tissues were determined by immunohistochemical analysis (bars = 20 μm).

moderately fractionated regimens (ie, 1.8-8 Gy per fraction) can provoke mitotic catastrophe, apoptosis, and autophagy, whereas high dose-per-fraction ablative HFRT induces necroptosis.

Currently the mechanisms underlying necroptosis are under investigation, and interference with necroptosis could have therapeutic implications. For example, Meng et al (13) suggest that necroptosis may be executed by necrosomes, including RIP1, RIP3, and MLKL. In contrast, Wu et al (29) demonstrated that necroptosis was dependent on RIP3, and RIP1 was not always required (29). Moreover, RIP3 deficiency was theorized to contribute to necroptosis resistance in malignant melanoma (10), and RIP1 has been purported to act as an inhibitor of necroptosis under some conditions (30). Therefore, in our experiments, RIP3-overexpressing and RIP3-silent NSCLC cell lines were successfully constructed; next, the mechanism of cell death, the number of colonies, and the regulated proteins of necroptosis were characterized in vitro and in vivo.

We found that the NSCLC cell lines LTEP-A2 and SPC-A1 both had robust RIP3 expression, as determined by Western blot assays. In contrast, the A549 cell line is

known to lack the expression of RIP3 and was therefore used in this study as a control in vitro. Our results demonstrate that resistance to HFRT is exhibited by A549 cells, and this resistance is induced by RNAi-RIP3 or pretreatment with Nec-1 in LTEP-A2 and SPC-A1 cell lines at ablative HFRT with ≥10 Gy per fraction. Furthermore, knockdown of RIP3 attenuates necroptosis after ablative HFRT in vivo.

Clinically, Kaplan-Meier survival analysis indicates that high expression of RIP3 is associated with improved LC and PFS (all $P < .05$; Fig. 6A-D). Local control in this study is slightly lower than that of the Radiation Therapy Oncology Group 0813 trial (17, 18), in part because eligible central early-stage NSCLC patients received individualized risk-adapted RT that maximized dose to the tumor while trying to attain all dose constraints. Therefore, RIP3 may serve as a useful biomarker to predict favorable response to SBRT if it can be validated in larger, prospective studies. In other words, despite demonstrating equivalent outcomes, lobectomy is still considered the standard of care for medically operative patients with stage I NSCLC. If validated, a predictive biomarker such as tumoral RIP3 expression could identify patients who may be better
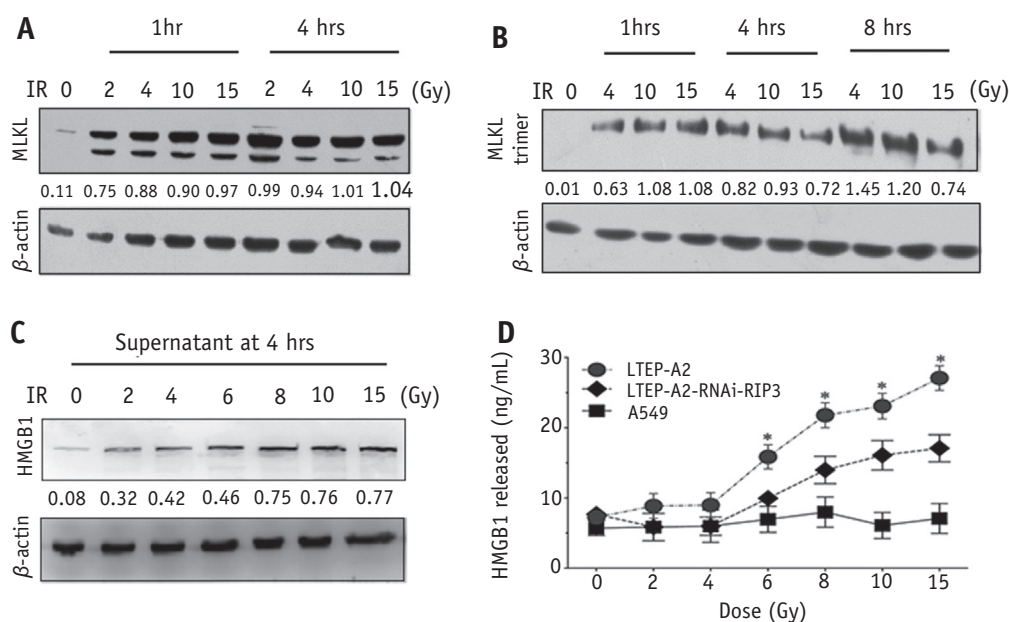
Fig. 5. Induction and activation of MLKL as well as release of HMGB1 were involved in ablative hypofractionated radiation therapy—induced necroptosis in vitro and in vivo. (A, B) LTEP-A2 cells were exposed to various doses of radiation therapy; next, MLKL induction and MLKL trimerization expression levels were evaluated by Western blot assays. (C, D) A549, LTEP-A2, and LTEP-A2 with RNAi-RIP3 xenograftic mice were exposed to various doses of radiation therapy, serum was obtained, and the release of HMGB1 was determined by enzyme-linked immunosorbent assay. *$P < .05$ versus LTEP-A2 + RNAi-RIP3.

managed with SBRT. Further studies should investigate whether an activator of RIP3 or its downstream effectors may be used clinically to radiosensitize tumor cells to ablative HFRT with doses ≥10 Gy per fraction.

Furthermore, MLKL induction and activation were identified as a critical downstream effector of RIP3 during the execution of necroptosis, and our results showed that RT significantly induced MLKL induction and activation in vitro and in vivo. Activity of MLKL was significantly decreased in NSCLC cells with RNAi-RIP3 and in cells without expression of RIP3. Interestingly, recent studies suggested that MLKL expression could serve as a potential prognostic biomarker for patients with cancer of the pancreas (31), ovaries (32), and colon (33). Our understanding of the necroptosis pathway continues to evolve, and further studies are necessary to character its role after RT.

Cancer cell death after RT and/or chemotherapy may precede, trigger, or amplify immunity. Emerging evidence suggests that ablative HFRT elicits a pronounced antitumor immune effect (34-36). The immune response depends on the dose per fraction; higher doses per fraction (eg, >8-10 Gy) stimulate an immune response, whereas use of conventionally fractionated radiation therapy (ie, approximately 2 Gy per fraction) does not stimulate as profound an immune effect and may contribute to subsequent death of lymphocytes that migrate to the tumor (37, 38). In this study we found that ablative HFRT with doses ≥10 Gy further resulted in the release of immune-activating molecule HMGB1, and therefore the treated tumor cells could stimulate an antitumoral response.

However, uncontrolled necroptosis could potentially cause irreversible tissue damage (39), and the immune inflammatory cells recruited by the inflammatory factors released by necrotic cells may promote angiogenesis and cancer cell proliferation (40). If invasive tumors tolerate necrosis, they may gain growth-stimulating factors from the recruited tumor-promoting inflammatory cells (41). The immunomodulatory properties of ablative HFRT, such as CD8+ T-cell infiltration of tumors, merit further investigation.

There are limitations to this study. First, there is no broad consensus defining cell death, including its mechanism, timing, or association with dose of ablative HFRT. This is in part because many of the pathways that influence cell death are unknown, vary among cell types, exist among a spectrum, and are difficult to assess individually. Second, it is unclear how necroptosis differs from necrosis, and we assessed them as a single mechanism in our experiments. Necroptosis is a broad term, its pathways are yet to be validated and defined, and new tools are needed to differentiate apoptosis from necroptosis (42). Third, the clonogenic formation assay is very difficult to perform at ablative HFRT, and the results should be repeated in other tumor cells and interpreted with caution. Additionally, it is unclear how other intracellular (eg, PKM2, RAS, TGF-β) (43, 44) and extracellular (eg, pericytes, mesenchymal stem cells) components (45, 46) may contribute to necroptosis.
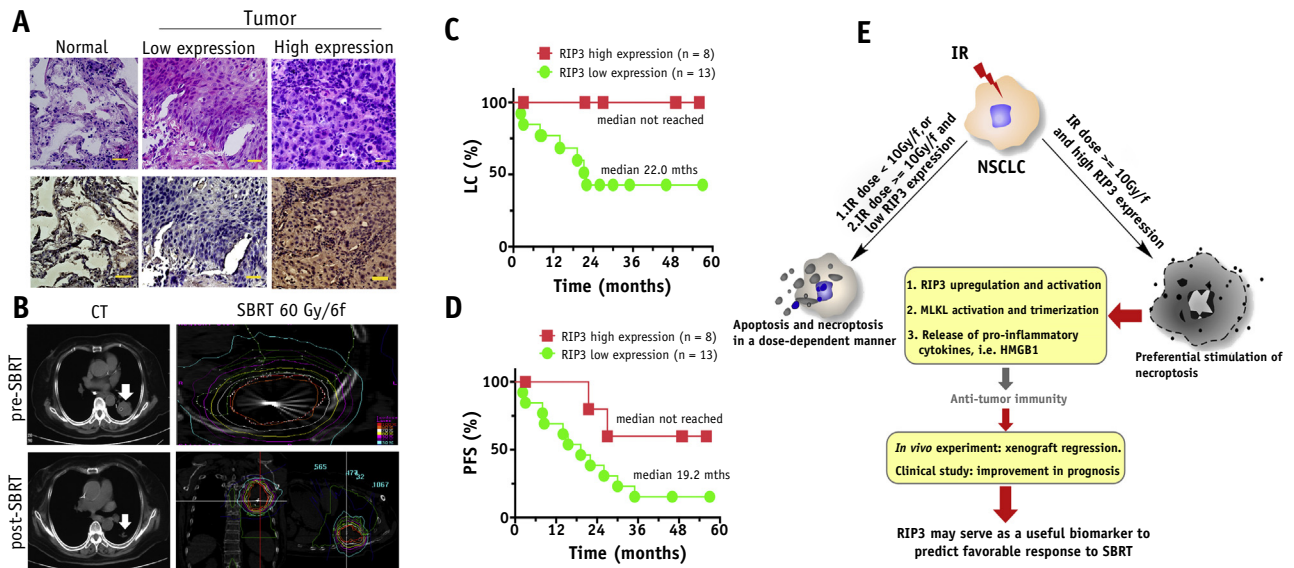
Fig. 6. Immunohistochemistry and hematoxylin-eosin (HE) of patient specimens, local control and progression-free survival, and diagrammatic illustrations of signaling pathways involved. (A) Representative images of RIP3 immunohistochemical (IHC) staining in early-stage non-small cell lung cancer tissues (magnification ×400, bar = 20 μm). Normal: a correspondent normal lung tissue (case 3) shows no expression of RIP3 (IHC score: 0). Low expression: a non-small cell lung cancer tissue (case 17) exhibited low expression of RIP3 (IHC score: 2). High expression: a non-small cell lung cancer tissue (case 12) exhibited high expression of RIP3 (IHC score: 16). (B) A 78-year-old woman presented with worsening cough for more than 2 years. Computed tomography revealed a central mass (3.2 × 2.5 cm) without lymph node metastasis, and fine-needle aspiration tissues demonstrated a lung adenocarcinoma with high RIP3 expression. She received stereotactic body radiation therapy at 60 Gy/6 fractions. Two months later, a 1.5 × 1-cm nodule was noted at the site of stereotactic body radiation therapy. She underwent lobectomy, and the final pathology showed fibrosis without tumor. (C, D) Kaplan-Meier survival analyses of local control (LC) and progression-free survival (PFS) were divided by the RIP3 expression levels. (E) Diagrammatic illustrations of signaling pathways involved. Radiation therapy at <10 Gy per fraction or ablative hypofractionated radiation therapy (HFRT) ≥10 Gy per fraction with low expression of RIP3-induced apoptosis and necroptosis in a dose-dependent manner; in contrast, ablative HFRT ≥10 Gy per fraction with high expression of PIP3 preferentially stimulated necroptosis, accompanied by enhanced MLKL induction and activation as well as HMGB1 release in vitro and in vivo. These results will inform our understanding of radiation biology after ablative HFRT.

Mitotic catastrophe is considered to be the primary mechanism of cell death after RT, with subsequent senescence and cell death by autophagy, apoptosis, or necrosis. This classification system has been disputed; for example, mitotic catastrophe has been reported to be fundamentally different from apoptosis but has also been classified as a special type of apoptosis (47). Given the discrepancies in definition of cell death and the variability of cell death among different cell types, we therefore focused on the 2 best-known regulated forms of tumor cell death: apoptosis and necroptosis. Notably we did not show that inhibition of apoptosis does not also render tumor cells resistant to hypofractionated doses, as it does with conventionally fractionated RT. Further studies are necessary to demonstrate that modulation of apoptosis has less effect on tumor cell survival (or ideally tumor growth delay in vivo) after HFRT than modulation of necroptosis, and further studies are warranted to assess a role of cross-talk among these tumor cell death modes. The forms of possible cell death along the dose fractionation spectrum are summarized in Figure E5 (available online at www.redjournal.org).

In conclusion, our results revealed that ablative HFRT at ≥10 Gy per fraction enhances killing of NSCLC with high RIP3 expression via preferential stimulation of necroptosis. RIP3 may serve as a useful biomarker to predict favorable response to SBRT if it can be validated in larger, prospective studies. These findings provide further understanding of radiation biology after SBRT and potential mechanisms to improve the therapeutic ratio.

References

1. Timmerman R, Paulus R, Galvin J, et al. Stereotactic body radiation therapy for inoperable early stage lung cancer. *JAMA* 2010;303:1070-1076.
2. Nuyttens JJ, van der Voort van Zyp NC, Praag J, et al. Outcome of four-dimensional stereotactic radiotherapy for centrally located lung tumors. *Radiother Oncol* 2012;102:383-387.
3. Okada H, Mak TW. Pathways of apoptotic and non-apoptotic death in tumor cells. *Nat Rev Cancer* 2004;4:592-603.
4. Olive PL, Frazer G, Banath JP. Radiation-induced apoptosis measured in TK6 human B lymphoblast cells using the comet assay. *Radiat Res* 1993;136:130-136.

5. Olive PL, Vikse CM, Vanderbyl S. Increase in the fraction of necrotic, not apoptotic, cells in SiHa xenograft tumors shortly after irradiation. *Radiother Oncol* 1999;50:113-119.

6. Hanahan D, Weinberg RA. Hallmarks of cancer: The next generation. *Cell* 2011;144:646-674.

7. Linkermann A, Green DR. Necroptosis. *N Engl J Med* 2014;370:455-465.

8. Degterev A, Hitomi J, Germscheid M, et al. Identification of RIP1 kinase as a specific cellular target of necrostatins. *Nat Chem Biol* 2008;4:313-321.

9. Zhang DW, Shao J, Lin J, et al. RIP3, an energy metabolism regulator that switches TNF-induced cell death from apoptosis to necrosis. *Science* 2009;325:332-336.

10. Geserick P, Wang J, Schilling R, et al. Absence of RIPK3 predicts necroptosis resistance in malignant melanoma. *Cell Death Dis* 2015;6:e1884.

11. Sun L, Wang H, Wang Z, et al. Mixed lineage kinase domain-like protein mediates necrosis signaling downstream of RIP3 kinase. *Cell* 2012;148:213-227.

12. Sims GP, Rowe DC, Rietdijk ST, et al. HMGB1 and RAGE in inflammation and cancer. *Annu Rev Immunol* 2010;28:367-388.

13. Meng MB, Wang HH, Cui YL, et al. Necroptosis in tumorigenesis, activation of anti-tumor immunity, and cancer therapy. *Oncotarget* 2016;7:57391-57413.

14. Fulda S. Therapeutic exploitation of necroptosis for cancer therapy. *Semin Cell Dev Biol* 2014;35:51-56.

15. Su Z, Yang Z, Xie L, et al. Cancer therapy in the necroptosis era. *Cell Death Differ* 2016;23:748-756.

16. Zhang J, Wang X, Cui W, et al. Visualization of caspase-3-like activity in cells using a genetically encoded fluorescent biosensor activated by protein cleavage. *Nat Commun* 2013;4:2157.

17. Bezjak A, Paulus R, Gaspar LE, et al. Primary study endpoint analysis for NRG Oncology/RTOG 0813 trial of stereotactic body radiation therapy (SBRT) for centrally located non-small cell lung cancer (NSCLC). *Int J Radiat Oncol Biol Phys* 2016;94:4-5.

18. Bezjak A, Paulus R, Gaspar LE, et al. Efficacy and toxicity analysis of NRG Oncology/RTOG 0813 trial of stereotactic body radiation therapy (SBRT) for centrally located non-small cell lung cancer (NSCLC). *Int J Radiat Oncol Biol Phys* 2016;94:S8.

19. Huang K, Senthi S, Palma DA, et al. High-risk CT features for detection of local recurrence after stereotactic ablative radiotherapy for lung cancer. *Radiother Oncol* 2013;109:51-57.

20. Brenner DJ. The linear-quadratic model is an appropriate methodology for determining isoeffective doses at large doses per fraction. *Semin Radiat Oncol* 2008;18:234-239.

21. Kirkpatrick JP, Meyer JJ, Marks LB. The linear-quadratic model is inappropriate to model high dose per fraction effects in radiosurgery. *Semin Radiat Oncol* 2008;18:240-243.

22. Wang JZ, Huang Z, Lo SS, et al. A generalized linear-quadratic model for radiosurgery, stereotactic body radiation therapy, and high-dose rate brachytherapy. *Sci Transl Med* 2010;2:39ra48.

23. Sheu T, Molkentine J, Transtrum MK, et al. Use of the LQ model with large fraction sizes results in underestimation of isoeffect doses. *Radiother Oncol* 2013;109:21-25.

24. Park C, Papiez L, Zhang S, et al. Universal survival curve and single fraction equivalent dose: Useful tools in understanding potency of ablative radiotherapy. *Int J Radiat Oncol Biol Phys* 2008;70:847-852.

25. McKenna FW, Ahmad S. Fitting techniques of cell survival curves in high-dose region for use in stereotactic body radiation therapy. *Phys Med Biol* 2009;54:1593-1608.

26. Song CW, Lee YJ, Griffin RJ, et al. Indirect tumor cell death after high-dose hypofractionated irradiation: Implications for stereotactic body radiation therapy and stereotactic radiation surgery. *Int J Radiat Oncol Biol Phys* 2015;93:166-172.

27. Pedicini P, Strigari L, Benassi M. Estimation of a self-consistent set of radiobiological parameters from hypofractionated versus standard radiation therapy of prostate cancer. *Int J Radiat Oncol Biol Phys* 2013;85:e231-e237.

28. Makris N, Edgren M, Mavroidis P, et al. Investigation of the dose- and time-dependence of the induction of different types of cell death in a small-cell lung cancer cell line: Implementation of the repairable-conditionally repairable model. *Int J Oncol* 2013;42:2019-2027.

29. Wu XN, Yang ZH, Wang XK, et al. Distinct roles of RIP1-RIP3 hetero- and RIP3-RIP3 homo-interaction in mediating necroptosis. *Cell Death Differ* 2014;21:1709-1720.

30. Orozco S, Yatim N, Werner MR, et al. RIPK1 both positively and negatively regulates RIPK3 oligomerization and necroptosis. *Cell Death Differ* 2014;21:1511-1521.

31. Colbert LE, Fisher SB, Hardy CW, et al. Pronecrotic mixed lineage kinase domain-like protein expression is a prognostic biomarker in patients with early-stage resected pancreatic adenocarcinoma. *Cancer* 2013;119:3148-3155.

32. He L, Peng K, Liu Y, et al. Low expression of mixed lineage kinase domain-like protein is associated with poor prognosis in ovarian cancer patients. *Onco Targets Ther* 2013;6:1539-1543.

33. Li X, Guo J, Ding AP, et al. Association of mixed lineage kinase domain-like protein expression with prognosis in patients with colon cancer. *Technol Cancer Res Treat* 2016;16:428-434.

34. Postow MA, Callahan MK, Barker CA, et al. Immunologic correlates of the abscopal effect in a patient with melanoma. *N Engl J Med* 2012;366:925-931.

35. Filatenkov A, Baker J, Mueller AM, et al. Ablative tumor radiation can change the tumor immune cell microenvironment to induce durable complete remissions. *Clin Cancer Res* 2015;21:3727-3739.

36. Popp I, Grosu AL, Niedermann G, et al. Immune modulation by hypofractionated stereotactic radiation therapy: Therapeutic implications. *Radiother Oncol* 2016;120:185-194.

37. Schaue D, Ratikan JA, Iwamoto KS, et al. Maximizing tumor immunity with fractionated radiation. *Int J Radiat Oncol Biol Phys* 2012;83:1306-1310.

38. Lugade AA, Moran JP, Gerber SA, et al. Local radiation therapy of B16 melanoma tumors increases the generation of tumor antigen-specific effector cells that traffic to the tumor. *J Immunol* 2005;174:7516-7523.

39. Gunther C, Martini E, Wittkopf N, et al. Caspase-8 regulates TNF-α-induced epithelial necroptosis and terminal ileitis. *Nature* 2011;477:335-339.

40. Grivennikov SI, Greten FR, Karin M. Immunity, inflammation, and cancer. *Cell* 2010;140:883-899.

41. Galluzzi L, Kroemer G. Necroptosis: A specialized pathway of programmed necrosis. *Cell* 2008;135:1161-1163.

42. Plemel JR, Caprariello AV, Keough MB, et al. Unique spectral signatures of the nucleic acid dye acridine orange can distinguish cell death by apoptosis and necroptosis. *J Cell Biol* 2017;216:1163-1181.

43. Meng MB, Wang HH, Guo WH, et al. Targeting pyruvate kinase M2 contributes to radiosensitivity of non-small cell lung cancer cells in vitro and in vivo. *Cancer Lett* 2015;356:985-993.

44. Palmer JD, Zaorsky NG, Witek M, et al. Molecular markers to predict clinical outcome and radiation induced toxicity in lung cancer. *J Thorac Dis* 2014;6:387-398.

45. Meng MB, Zaorsky NG, Deng L, et al. Pericytes: A double-edged sword in cancer therapy. *Future Oncol* 2015;11:169-179.

46. Wang HH, Cui YL, Zaorsky NG, et al. Mesenchymal stem cells generate pericytes to promote tumor recurrence via vasculogenesis after stereotactic body radiation therapy. *Cancer Lett* 2016;375:349-359.

47. Castedo M, Perfettini JL, Roumier T, et al. Mitotic catastrophe constitutes a special case of apoptosis whose suppression entails aneuploidy. *Oncogene* 2004;23:4362-4370.